Resolved ALMA Continuum Image of the Circumbinary Ring and Circumstellar Disks in the L1551 IRS 5 System

Fernando Cruz-Sáenz de Miera[1] , Ágnes Kóspál[1,2] , Péter Ábrahám[1] , Hauyu Baobab Liu[3] , and Michihiro Takami[3]

[1] Konkoly Observatory, Research Centre for Astronomy and Earth Sciences, Hungarian Academy of Sciences, Konkoly-Thege Miklós út 15-17, 1121 Budapest, Hungary; cruzsaenz.fernando@csfk.mta.hu
[2] Max Planck Institute for Astronomy, Königstuhl 17, D-69117 Heidelberg, Germany
[3] Institute of Astronomy and Astrophysics, Academia Sinica, 11F of Astronomy-Mathematics Building, AS/NTU, No.1, Sec. 4, Roosevelt Road, Taipei 10617, Taiwan, R.O.C.

Abstract

L1551 IRS 5 is a FUor-like object located in the Taurus star-forming region. We present Atacama Large Millimeter/submillimeter Array (ALMA) 1.3 mm continuum observations using a wide range of baselines. The observations recovered the two circumstellar disks comprising the system and, for the first time, resolved the circumbinary ring. We determined the geometry and estimated lower mass limits for the circumstellar disks using simple models. We calculated lower limits for the total mass of both circumstellar disks. After subtracting the two circumstellar disk models from the image, the residuals show a clearly resolved circumbinary ring. Using a radiative transfer model, we show that geometrical effects can explain some of the brightness asymmetries found in the ring. The remaining features are interpreted as enhancements in the dust density.

Key words: circumstellar matter – stars: individual (L1551 IRS 5) – stars: pre-main sequence

1. Introduction

Stellar multiplicity is widespread: although the multiplicity fraction decreases with age, it is possible that all stars are born in multiple systems (Duchêne & Kraus 2013; Reipurth et al. 2014). Some of these break up later due to dynamical interactions, but some survive for long enough to form circumbinary planets (Welsh et al. 2015). Such planets form in protoplanetary disks that may be substantially affected by the components of the stellar multiple system. For example, depending on the separation, disks may be truncated from the outside (in the case of a circumstellar disk) or from the inside (in the case of a circumbinary disk; Artymowicz & Lubow 1994). Eccentric binaries may induce spiral arms in the circumbinary disk (Mayama et al. 2010; Takakuwa et al. 2017; Wagner et al. 2018). While disk truncation may inhibit planet formation, there are indications that circumbinary disks may feed material to circumstellar disks, helping planet formation (Dutrey et al. 2014; Boehler et al. 2017). All these processes and structures may affect grain growth and, consequently, planet formation (Price et al. 2018).

In order to understand the details of disk evolution and planet formation in binary and multiple systems, observations of the disks' thermal emission are indispensable. If these observations have high spatial resolution, they can reveal the complex morphology of the circumstellar and circumbinary material, while data at multiple wavelengths help constrain the optical depth and the grain size distribution (Birnstiel et al. 2010; Testi et al. 2014; Woitke et al. 2016). Here we present 1.3 mm, high spatial resolution observations of the young binary L1551 IRS 5 taken with the Atacama Large Millimeter/submillimeter Array (ALMA). We analyze the structure of the cold material in the system at 20 au resolution.

2. Our Target

L1551 IRS 5 is a deeply embedded very young ($\sim 10^5$ yr) system at a distance of 147 ± 5 pc classified as a FUor-like object by Connelley & Reipurth (2018). It consists of a 0.8 $M_\odot$ primary (N component), which dominates the system's luminosity, and a 0.3 $M_\odot$ secondary (S component), which is invisible at near-infrared wavelengths (Duchêne et al. 2007). The separation of the binary is $0\rlap.{''}36$ or 50 au (Liseau et al. 2005; Lim et al. 2016). Its total bolometric luminosity is in the range of 25–40 $L_\odot$ (Osorio et al. 2003; Liseau et al. 2005). Both stars accrete at a much higher rate than normal T Tauri stars ($\sim 10^{-8}$ $M_\odot$ yr^{-1}; e.g., Gullbring et al. 1998) with accretion rates of $\dot{M}_N = 6 \times 10^{-6}$ $M_\odot$ yr^{-1} and $\dot{M}_S = 2 \times 10^{-6}$ $M_\odot$ yr^{-1} (Liseau et al. 2005). The sources also drive powerful radio jets observed at 7 mm (Lim et al. 2016) and 3.5 cm (Rodríguez et al. 2003). According to the modeling of Osorio et al. (2003) the stars are surrounded by small but massive circumstellar (CS) disks (CS disk masses: $M_{\mathrm{disk,N}} = 0.25$ $M_\odot$, $M_{\mathrm{disk,S}} = 0.1$ $M_\odot$, CS disk radii about 12 au at 7 mm), a circumbinary (CB) ring (CB ring mass: 0.4 $M_\odot$), and an envelope (envelope mass: 4 $M_\odot$). Both CS disks have similar inclinations (45°) and position angles (150°; Lim et al. 2016).

3. Observations and Data Reduction

We observed L1551 IRS 5 in ALMA Cycle 4 (ID: 2016.1.00209.S; PI: Takami) with the 7 m array using 11 antennas with projected baselines between 8.9 and 45 m on 2016 November 14, with the 12 m array in compact configuration using 44 antennas with projected baselines between 15 and 500 m on 2018 April 24, and in extended configuration using 44 antennas with projected baselines between 30.5 m and 3.6 km on 2017 July 24. Data were taken in Band 6, with three spectral windows centered at the ^{12}CO (at 30 kHz resolution), ^{13}CO and C^{18}O $J = 2 - 1$ lines (at 60 kHz resolution), and two continuum spectral windows of 1875 MHz bandwidth each, centered at 216.9 and 232.2 GHz. Here we present the results of the continuum data; the analysis of line data will be presented in a later publication. The data sets were calibrated using CASA v.5.1.1 (McMullin et al. 2007). We

applied self-calibration for both the visibility phases and amplitudes to improve signal-to-noise ratio (S/N). The common baselines between the three different observing configurations were consistent, therefore we concatenated them into a single data set that recovers the emission in all spatial scales. After excluding the channels with line emission from the combined data set, we created continuum images by cleaning using uniform and natural weighting. For the uniform image the resulting synthesized beam size is $0\rlap.''144 \times 0\rlap.''102$ (21 au × 15 au), while the rms noise is 0.33 mJy beam^{-1}. In the case of the natural image the resulting synthesized beam size is $0\rlap.''198 \times 0\rlap.''183$ (29 au × 27 au), while the rms noise is 0.76 mJy beam^{-1}.

4. Structures in the Continuum Map

Figures 1(a), (b) show the 1.3 mm continuum emission map of L1551 IRS 5 with the uniform and natural weighting schemes, respectively. The binary system and its circumbinary material are clearly detected. Based on the high S/N of our detections, we aimed to estimate geometrical properties of the CS disks based on the deconvolution of 2D Gaussians. We used CASA's IMFIT tool to fit both CS disks simultaneously using a single 2D Gaussian for each disk. We estimated the disks radii from the half-width half-maximum assuming a distance to the system of 147 ± 5 pc. The disk inclinations were calculated from the ratio between the semi-axes and the position angles were directly taken from the deconvolved parameters. Our results for the two CS disks are presented in Table 1. We found that both disks are marginally resolved and their estimated radii indicate that both CS disks are fairly compact. The resulting inclination and position angles are better constrained in the N disk, which is not surprising due to its slightly larger radius (Lim et al. 2016). However, as we show below, there are indications that the emission from our CS disks is mixed with other components, which cannot be resolved with the angular resolution of our current observations, and cause the large uncertainties in our fitting results. From the centroids of our 2D Gaussian function we estimated the separation between the two protostars to be 365 ± 4 mas (51 ± 0.6 au); this separation is in agreement with the orbital analysis by Lim et al. (2016).

After removing the contribution from the fitted 2D Gaussians, the residuals showed that a single component was not enough to describe the emission from each CS disk, similar to the case of the 7 mm VLA observations of L1551 IRS 5 (Lim et al. 2016). We followed a procedure similar to Lim et al. (2016) and used two 2D Gaussians to describe each CS disk and found that the positions of the components are similar to those found in Lim et al. (2016), which were attributed to jet emission. However, due to the beam size of our observations we are not able to clearly disentangle the emission from the CS disks and possible contribution from the jets; therefore, we cannot make a proper comparison between our results and those of Lim et al. (2016).

In Panels (e) and (f) of Figure 1 we show the residuals after subtracting the four best-fitted 2D Gaussians describing the CS disks. In both residuals, we see extended CB emission that had been reported in previous works (e.g., Chou et al. 2014; Liu et al. 2018). However, the present ones are the first resolved observations of the CB material. We estimated the radius, inclination, and position angle of the extended emission by

fitting an ellipse to all pixels above 12σ in the residual images. These results are also shown in Table 1.

Residuals in both the uniformly and naturally weighted maps show a bright source slightly to the north of the position of the CS N disk. It has a peak emission of ∼13 and ∼43 mJy beam^{-1} for the uniform and natural residuals, respectively. This source had not been detected previously; further analysis of this component is beyond the scope of this Letter and will be presented in a follow-up paper.

The residuals show less emission in the center of the image, indicating the presence on a CB ring. This is more clearly seen in the uniform residuals (e), than in the natural residuals (f), due to the difference in beam sizes. However, in both cases, the northern region of the CB ring is brighter than the southern region, which appears to be more extended.

In the top row of Figure 2 we show the deprojected residuals for both weighting schemes. We began by using a 2D Gaussian to remove the bright source from panels (e) and (f) of Figure 1, we rotated the remaining emission based on the position angle of the CB emission and deprojected the residuals using the inclination angles of the CB rings. In the bottom row of Figure 2 we show the azimuthally averaged radial profiles of both deprojected residuals. We estimated the width of the ring by fitting a 1D Gaussian to the peak of the radial profiles and deconvolved them by their respective beams. We found that the ring peaks at 100 ± 1 au and has a width of 38 ± 0.6 au.

In both weighting schemes, the residuals show the CB ring surrounded by faint emission, which is interpreted as the dust contribution from the system's extended envelope.

5. Analysis

5.1. Photometry and In-band Spectral Indices

We calculated the photometry of the two CS disks and the CB ring for both weighting schemes. In the case of the CS disks, the photometry was done by integrating all emission inside of the fitted single-component 2D Gaussians. In the case of the CB ring, we used the residuals, shown in Figures 1(e), (f), and an elliptical annulus aperture with inner radius of 46 au and outer radius of 285 au with an inclination angle of 45° and a position angle of 161°. The calculated fluxes are presented in Table 1. The total flux of the two CS disks and the CB ring is similar to the 1.3 mm SMA fluxes presented by Liu et al. (2018), which did not resolve the individual components.

We used the visibilities of our two continuum spectral windows to estimate the spectral index α using

$$\alpha = \frac{\ln(F_{\nu_1}) - \ln(F_{\nu_2})}{\ln(\nu_1) - \ln(\nu_2)}, \tag{1}$$

where $\nu_1 = 232.2$, $\nu_2 = 216.9$ GHz, and F_ν is the amplitude for each spectral window. We found that the longer baselines have $\alpha \approx 2$, while the shorter baselines have α values between 2 and 3. The smaller value of α for the shorter spatial scales can be an indication of the presence of larger dust grains in the CS disks or that the system becomes optically thick at these short spatial scales. We note that because the continuum spectral window frequencies are too close together, there are large uncertainties in the estimation of the spectral index. However, the high S/N of our observations provides enough to perform a comparative analysis between the short and long baselines.
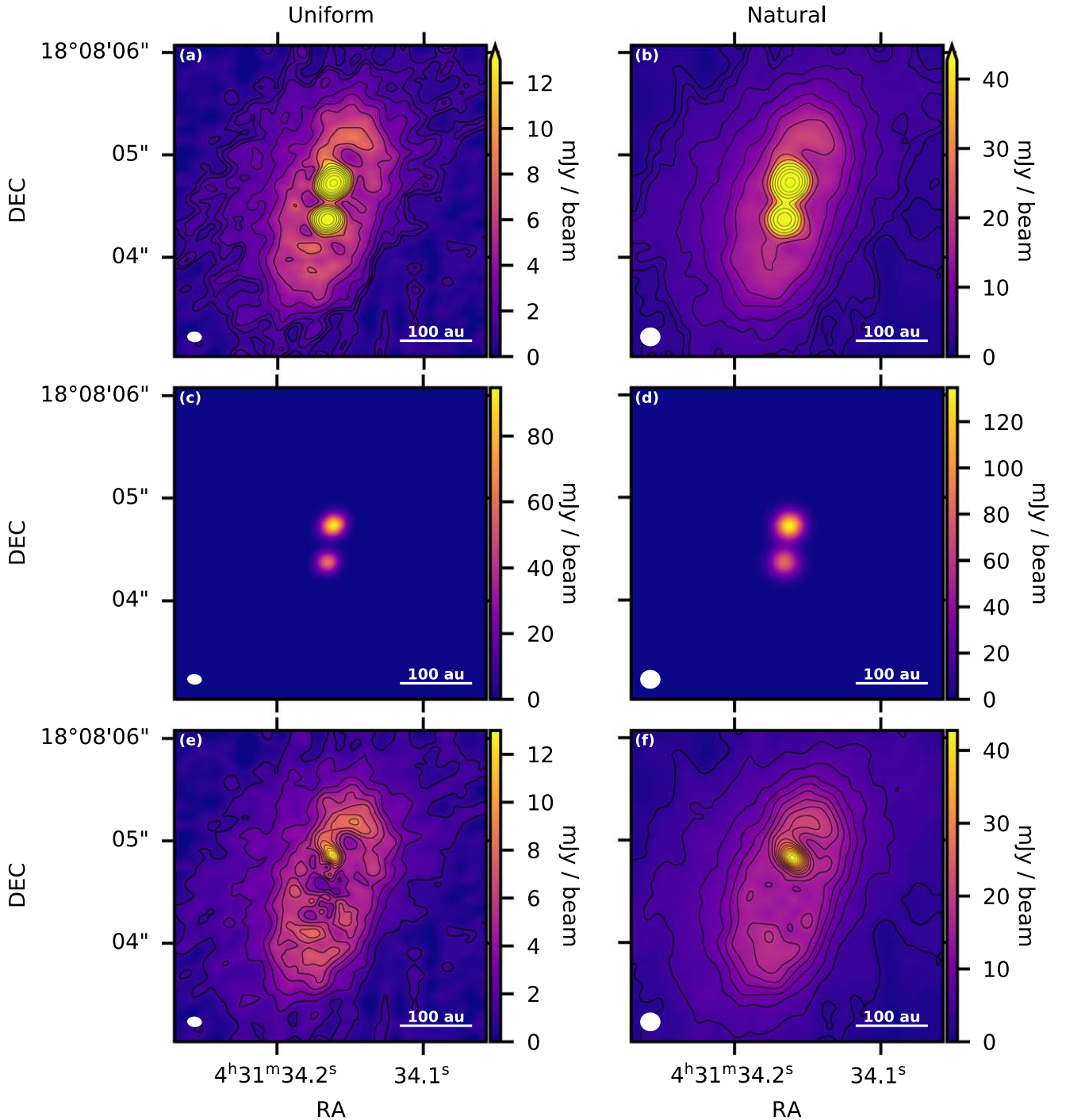
Figure 1. 1.3 mm continuum ALMA images of L1551 IRS 5. The left and right columns are the uniform and natural weighted images, respectively. The synthesized beam is shown in the bottom-left corner of each panel. Panels (a), (b) show the complete flux range in logarithmic scale. The uniform contours range from 3 to 283σ and the natural contours range from 3 to 205σ, in both cases the contours are in logarithmic steps. Panels (c), (d) show the 2D Gaussian disk models for the CS disks. Panels (e), (f) show the residuals after subtracting the contribution from the CS disks. The uniform contours range from 3 to 36σ and the natural contours range from 3 to 56σ, in both cases the contours are in steps of 3σ.

For completeness, we calculated the α index using the 7 mm ($\sim$43 GHz) VLA observations from Lim et al. (2016) and our uniformly weighted integrated fluxes. We obtained values of 2.32 ± 0.03 and 2.26 ± 0.04 for the north and south disks, respectively.

5.2. Mass Estimates for the Components

The disks around FUor stars are more massive than the disks around T Tauri stars (Cieza et al. 2018). Because the previously mentioned α index values indicate that our disks are probably optically thick, our mass estimates must be interpreted as conservative lower limits. We calculated the dust masses using

Table 1
Modeling Results of the Components of the L1551 IRS 5 System

Weighting	Radius (au)	Inclination (deg)	Position Angle (deg)	Peak Flux (mJy beam^{-1})	Integrated Flux (mJy)	Disk Mass ($M_\odot$)
North						
Natural	13.3 ± 3.5	35 ± 14	169 ± 31	146.0 ± 7.0	304 ± 22	$>6.03 \times 10^{-3}$
Uniform	10.3 ± 1.8	40 ± 9	156 ± 16	92.5 ± 2.9	236 ± 10	$>4.68 \times 10^{-3}$
South						
Natural	14.0 ± 5.0	45 ± 15	80 ± 60	89.0 ± 7.0	178 ± 21	$>5.76 \times 10^{-3}$
Uniform	8.8 ± 2.7	24 ± 25	110 ± 70	59.7 ± 2.9	137 ± 9	$>4.44 \times 10^{-3}$
CB Ring						
Natural	141.9 ± 7.4	61.5 ± 1.7	162 ± 2	$\cdots$	729.9 ± 81.9	2.99×10^{-2}
Uniform	136.8 ± 6.1	59.5 ± 1.4	161 ± 2	$\cdots$	474.5 ± 29.9	1.95×10^{-2}

the following formula:

$$M_{\text{dust}} = \frac{f\, d^2}{\kappa\, B_\nu(T_{\text{dust}})}, \qquad (2)$$

where f is the integrated flux, d is the distance (147 ± 5 pc), κ is the dust opacity ($0.22\,\text{m}^2\,\text{kg}^{-1}$), and T_{dust} is the dust temperature. We calculated the brightness temperature for the peak of each CS disk and used it as an approximation of the dust temperatures for the CS disks: $T_{\text{dust,N}} = 160\,\text{K}$ and $T_{\text{dust,S}} = 100$ K. For the CB ring we used $T_{\text{dust,R}} = 80$ K, which is the dust temperature at the characteristic radius of our radiative transfer model (see below). Assuming a 100:1 gas-to-dust mass ratio, we calculated the total disk mass for each component, and the results are presented in Table 1. These mass lower limits could increase by a factor of up to 3 due to beam dilution effects. In the following section, we present a comparison our mass lower limits with the mass estimates from other FUor disks.

5.3. Structure of the CB Ring

In panels (e) and (f) of Figure 1 we show the residuals after the removal of the CS disk contributions for the uniform and natural weighting schemes, respectively. As mentioned earlier, the brighter areas in the northern and southern parts of the circumbinary emission are due to geometrical effects of an inclined optically thin dust ring.

We tested this scenario by building radiative transfer models using RADMC-3D[4] (Dullemond et al. 2012) and comparing them with the natural weighted residuals. Each model was constructed using the parameterization presented in Andrews et al. (2009), in which the surface density was described as

$$\Sigma(R) = \Sigma_c \left(\frac{R}{R_c}\right)^{-\gamma} \exp\left[-\left(\frac{R}{R_c}\right)^{2-\gamma}\right], \qquad (3)$$

where R_c is the characteristic radius, γ is the surface density gradient, and Σ_c is the surface density at the characteristic

radius, which is given by

$$\Sigma_c = (2 - \gamma)\frac{M_{\text{dust}}}{2\pi R_c^2}. \qquad (4)$$

Finally, the scale height is described as $H_R = R\, h$, where h is the normalized scale height defined as

$$h = h_c \left(\frac{R}{R_c}\right)^\psi, \qquad (5)$$

where h_c is the scale height at R_c, and ψ indicates the disk flaring. The models were generated using two heating sources with $T_* = 10{,}000$ K and $R_* = 2\,R_\odot$; these values are roughly equivalent to the total bolometric luminosity of the system and are representative of the enhanced accretion rate. We fixed the positions of the two heating sources to the peak emission of each CS disk, and assumed the heating sources and the CB ring to be in the same plane. We constructed images based on each model using the best-fitted inclination and position angles presented in Table 1.

We searched for the best-fitting model by running a Markov chain Monte Carlo (MCMC) using the EMCEE Python module (Foreman-Mackey et al. 2013) to explore the parameter space and maximize the likelihood function.

In Figure 3 we present the natural weighted image, the convolved best-fitted model, and the respective residuals. The residuals show emission in the inner parts of the CB ring, which can be explained by dust in the inner cavity, and explain why our fitted characteristic ring radius of $R_c = 110.9^{+0.12}_{-0.18}$ au is larger than the peak in the radial profile found in Figure 2. Additionally, there is positive residual emission north and south of the CS disks and negative residuals to the east of the position of the CB ring; these can be explained by a non-axisymmetric dust distribution and will require more detailed modeling. Finally, there are two areas with a $\leqslant 4\sigma$ significance in the northeast and southwest of the residual map, which are attributed to emission from the envelope.

6. Discussion

L1551 IRS 5 is a FUor-like system with two CS disks of the same age and, therefore, presents an interesting opportunity to compare the two disks. The northern disk is ~ 2 times brighter and only slightly larger than the southern disk, therefore we interpret this as an indicative that the northern source is the

---

4   http://www.ita.uni-heidelberg.de/~dullemond/software/radmc-3d/
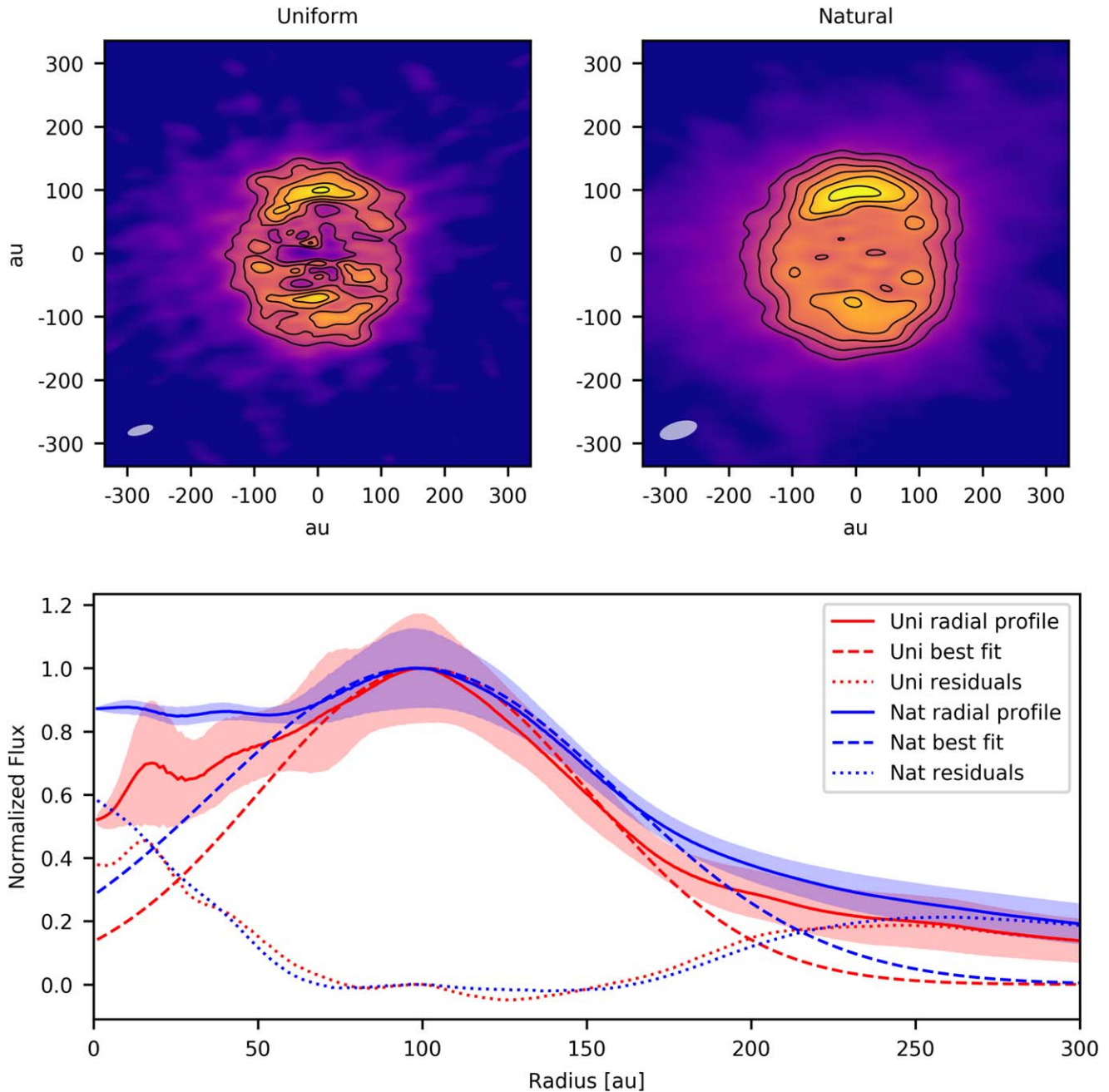
Figure 2. Top row: deprojected maps of the uniform and natural residuals, after the removal of the CS disks and the remaining bright source. The contours range from 12σ to 24σ and 27σ for the uniform and natural images, respectively, with steps of 3σ. Bottom row: radial profiles of the deprojected residuals (solid lines), best-fitted 1D Gaussian (dashed lines), and the residuals (dotted lines).

eruptive star. This is supported by L-band observations presented by Duchêne et al. (2007), which showed the northern disk as a point-like source with a surrounding nebulosity and did not detect the southern source.

We put the CS disks of L1551 IRS 5 into context by comparing their sizes and masses to the sample presented in Cieza et al. (2018), where they analyzed eight young eruptive stars in contrast to a sample of T Tauri stars previously presented by Andrews et al. (2010). Our measured radii, presented in Table 1, indicate that the L1551 IRS 5 CS disks are smaller than the resolved sources in the Cieza et al. (2018) sample. The lower limits for the disk masses of each CS disk fall within the range of expected masses of T Tauri stars with small radii (Figure 6 of Cieza et al. 2018). However, because

the CS disks in L1551 IRS 5 could be optically thick, it is possible that we are underestimating their total masses by up to 90% (Liu et al. 2018), which would place the L1551 IRS 5 CS disks masses with what is expected from other FUor-like systems.

Tobin et al. (2018) analyzed a sample of 17 Class 0 and Class I multiple-star systems with separations of less than 600 au using ALMA 1.3 mm and VLA 9.1 mm data. They did not detect circum-multiple dust emission around any of the Class I systems; however, closer binaries are more likely to have CB material (Bate 2000) and the closest separation for Class I systems in their sample is $\sim$90 au. The in-band α spectral index values for the L1551 IRS 5 CS disks are similar to the spectral indexes presented by Tobin et al. (2018).
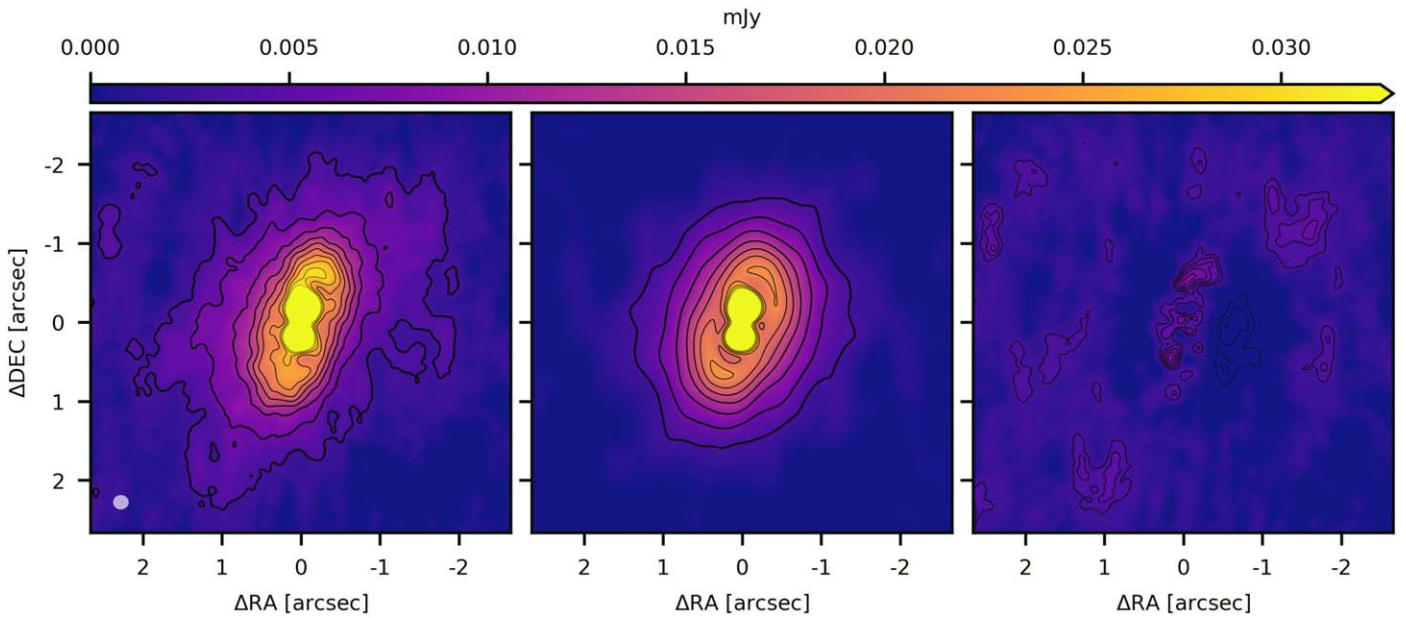
Figure 3. Radiative transfer modeling of the CB ring based on the natural weighted image of L1551 IRS 5. The colorscale is saturated at 30σ to show the structured of the CB material. The left panel shows our observations. The middle panel shows the best-fit model convolved with the clean beam. The right panel shows the differences between the observations and the best-fit model. The overplotted contours are from 3 to 27σ in steps of 2σ.

L1551 NE is a Class I protostellar binary system with a similar morphology to L1551 IRS 5: two CS disks, with a 70 au separation, and a CB ring. Based on the ALMA 0.9 mm continuum images from Takakuwa et al. (2017), the biggest difference between the two systems is in their CB ring brightness distribution. Contrary to the relative axisymmetry of the L1551 IRS 5 CB ring, the western side of L1551 NE is much brighter than its eastern side, which only shows a few small clumps of material. Additionally, the CS disks in L1551 NE are misaligned and not coplanar with the CB ring, which the authors suggested as an indication that the outer material from the CB ring is falling directly into the surfaces of the CS disks, instead of smoothly connecting with the outer parts of the disks.

7. Summary

In this work we have presented ALMA 1.3 mm continuum observations of L1551 IRS 5, a FUor-like object made up of two low-mass stars, each with a CS disk and a CB ring. The high resolution of our observations has enabled us to clearly separate the three components of this system.

Having two CS disks in the same FUor-like system opens up the possibility of analyzing each disk separately. From the marginally resolved detection of the CS disks, we measured their radii and found that both of them are smaller than any of the previously resolved FUors at this wavelength. The spectral index α indicated that the CS disks may be optically thick. We calculated conservative lower limits for the total disk masses and found that they are in accordance with the expected values of other known FUor disks.

Based on the residuals, the CB emission appears to be ring-shaped with a width of 38 ± 0.6 au. From our radiative transfer modeling, the CB ring appears to be mostly axisymmetric with a smooth surface density. We interpreted the more significant residuals as indication of small asymmetries in the CB dust distribution.

Due to the complexity of the system and its distance, complementary observations with higher angular resolution and at different frequencies are necessary to (1) fully analyze the circumstellar disks, including their optically thick inner parts, (2) verify the presence of the third bright component and study its nature, (3) study the asymmetries found in the circumbinary material.

ORCID iDs

Fernando Cruz-Sáenz de Miera ● https://orcid.org/0000-0002-4283-2185
Ágnes Kóspál ● https://orcid.org/0000-0001-7157-6275
Péter Ábrahám ● https://orcid.org/0000-0001-6015-646X
Hauyu Baobab Liu ● https://orcid.org/0000-0003-2300-2626
Michihiro Takami ● https://orcid.org/0000-0001-9248-7546

References

Andrews, S. M., Wilner, D. J., Hughes, A. M., Qi, C., & Dullemond, C. P. 2009, ApJ, 700, 1502

Andrews, S. M., Wilner, D. J., Hughes, A. M., Qi, C., & Dullemond, C. P. 2010, ApJ, 723, 1241

Artymowicz, P., & Lubow, S. H. 1994, ApJ, 421, 651

Astropy Collaboration, Robitaille, T. P., Tollerud, E. J., et al. 2013, A&A, 558, A33

Bate, M. R. 2000, MNRAS, 314, 33

Birnstiel, T., Ricci, L., Trotta, F., et al. 2010, A&A, 516, L14

Boehler, Y., Weaver, E., Isella, A., et al. 2017, ApJ, 840, 60

Chou, T.-L., Takakuwa, S., Yen, H.-W., Ohashi, N., & Ho, P. T. P. 2014, ApJ, 796, 70

Cieza, L. A., Ruíz-Rodríguez, D., Perez, S., et al. 2018, MNRAS, 474, 4347

Connelley, M. S., & Reipurth, B. 2018, ApJ, 861, 145

Duchêne, G., Bontemps, S., Bouvier, J., et al. 2007, A&A, 476, 229

Duchêne, G., & Kraus, A. 2013, ARA&A, 51, 269

Dullemond, C. P., Juhasz, A., Pohl, A., et al. 2012, RADMC-3D: A Multi-purpose Radiative Transfer Tool, RADMC3D Version 0.41, Astrophysics Source Code Library, ascl:1202.015

Dutrey, A., di Folco, E., Guilloteau, S., et al. 2014, Natur, 514, 600

Foreman-Mackey, D., Hogg, D. W., Lang, D., & Goodman, J. 2013, PASP, 125, 306

Gullbring, E., Hartmann, L., Briceño, C., & Calvet, N. 1998, ApJ, 492, 323

Lim, J., Yeung, P. K. H., Hanawa, T., et al. 2016, ApJ, 826, 153

Liseau, R., Fridlund, C. V. M., & Larsson, B. 2005, ApJ, 619, 959

Liu, H. B., Dunham, M. M., Pascucci, I., et al. 2018, A&A, 612, A54

Mayama, S., Tamura, M., Hanawa, T., et al. 2010, Sci, 327, 306

McMullin, J. P., Waters, B., Schiebel, D., Young, W., & Golap, K. 2007, in ASP Conf. Ser. 376, Astronomical Data Analysis Software and Systems XVI, ed. R. A. Shaw, F. Hill, & D. J. Bell (San Francisco, CA: ASP), 127

Osorio, M., D'Alessio, P., Muzerolle, J., Calvet, N., & Hartmann, L. 2003, ApJ, 586, 1148

Price, D. J., Cuello, N., Pinte, C., et al. 2018, MNRAS, 477, 1270

Reipurth, B., Clarke, C. J., Boss, A. P., et al. 2014, in Protostars and Planets VI, ed. H. Beuther et al. (Tucson, AZ: Univ. Arizona Press), 267

Rodríguez, L. F., Porras, A., Claussen, M. J., et al. 2003, ApJL, 586, L137

Takakuwa, S., Saigo, K., Matsumoto, T., et al. 2017, ApJ, 837, 86

Testi, L., Birnstiel, T., Ricci, L., et al. 2014, in Protostars and Planets VI, ed. H. Beuther et al. (Tucson, AZ: Univ. Arizona Press), 339

Tobin, J. J., Looney, L. W., Li, Z.-Y., et al. 2018, ApJ, 867, 43

Wagner, K., Dong, R., Sheehan, P., et al. 2018, ApJ, 854, 130

Welsh, W. F., Orosz, J. A., Short, D. R., et al. 2015, ApJ, 809, 26

Woitke, P., Min, M., Pinte, C., et al. 2016, A&A, 586, A103